Materials Characterization 180 (2021) 111443

Contents lists available at ScienceDirect

Materials Characterization

journal homepage: www.elsevier.com/locate/matchar

Microstructure and precipitation behavior of advanced RAFM steels for high-temperature applications on fusion reactors

P. Fernández [a,*], J. Hoffmann [b], M. Rieth [b], A. Gómez-Herrero [c]

[a] CIEMAT, National Fusion Laboratory, Technology Division, Avda. Complutense, 40, 28040 Madrid, Spain
[b] Karlsruhe Institute of Technology, Campus Nord, Institute for Applied Materials, P.O. Box 3640, 76021 Karlsruhe, Germany
[c] National Center of Electronic Microscopy, Av. Complutense s/n, 28040 Madrid. Spain

ARTICLE INFO

Keywords:
Advanced steels
Microstructure
Secondary phases
STEM
EELS

ABSTRACT

The composition of new eigth 9% Cr reduced activation ferritic/martensitioc steels (RAFMs) has been finely tuned in order to increase the amount of fine MX precipitates and reduce coarse $M_{23}C_6$ carbides through the application of thermomechanical treatments. The microstructural investigations by TEM/STEM and EELS have shown $M_{23}C_6$, M_2X (Cr_2N), and MX (Ta, V, and Ti-rich) precipitates after tempering at 750 °C/2 h. Higher N contens (0.04–0.03 wt%) seems to favored M_2X precipitation over MX with V contents round 0.2 wt%. MX-Ti rich presents sizes larger than MX (Ta or V rich). EELS anlysis have shown that the MX (Ta, V and Ti rich) precipitated after tempering at 750 °C/2 h are mainly carbo-nitrides. Composition, size, number density and carbon and nitrogen content on MX and M_2X is discussed in terms of the composition of each Alloy.

1. Introduction

At present, to increase the thermal efficiency of the next generation of nuclear reactors (fission and fusion) requires the use of materials able to maintain structural integrity in hard radiation environments at high temperatures. Especially on fusion energy systems to ensure safety margins, the materials need to sustain intense heat fluxes, significant cyclic thermomechanical stresses, corrosive breeders, and intense fluxes of neutrons and electromagnetic radiation.

Reduced Activation Ferritic/Martensitic steels (RAFMs) begin to develop in the mid-1980s when the research programs in Europe, Japan, and the United States began working in this kind of materials for use in a fusion energy demonstration reactor (DEMO) and subsequent power reactors [1–9]. After three decades of research and development, RAFM steels, candidate structural materials for fusion reactors, have achieved significant progress [10–12], converging to a nominal composition of 9%CrWVTa.

Advanced concepts of fusion power plants necessitate structural materials operating at high temperatures in order to achieve high thermodynamic efficiency, as well as at low temperatures dictated by the normal shutdown and start-up operations. A new generation of 9% Cr steels, advanced RAMFs, is being developed to improve the material performance of current RAFM steels at elevated temperatures focussed to increase the number density of nano-secondary phases to pin the lath boundaries and dislocations. During operation, the strength of this new generation will depend on the microstructural evolution of its initial tempered martensite microstructure and the secondary phases precipitated therein. It is well known that the precipitation process is dictated by the alloy composition and fabrication route.

Phase transformations or precipitation sequences taking place in the 9–12 wt% Cr steels have been described by many authors [13–21]. After tempering $M_{23}C_6$ and MX ("M showing the metal content and "X" as carbon and/or nitrogen) are the dominant secondary phases [14,18,22]. M_2X particles have also been observed on tempered microstructures of 9–12 Cr wt% alloys [16,21–23]. The microstructure of 9% Cr during long time service leads to aging-related microstructural evolution such as martensite laths growth, subgrains formation, and coarsening of $M_{23}C_6$ resulting in mechanical properties degradation. The current versions of RAFM steels, such as F82H and EUROFER97, contain relatively large amount of Cr-rich carbides ($M_{23}C_6$) precipitated at prior-austenite grain and martensite laths boundaries which cannot effectively pin the grain boundaries during deformation at high temperatures due to easier coarsening, and only limited amounts of MX to strengthen the matrix is present in current RAFM steels.

Thermomechanical treatments (TMTs) and alloy chemistry refinement are the primary routes to obtain superior performance at high

* Corresponding author.
E-mail address: pilar.fernandez@ciemat.es (P. Fernández).

https://doi.org/10.1016/j.matchar.2021.111443
Received 4 March 2021; Received in revised form 3 September 2021; Accepted 4 September 2021
Available online 8 September 2021

Table 1
Chemical composition (wt%) of Advanced RAFM steels studied.

	K465A	K468A	K473A	K476A	K466A	K469A	K471A	K474A
C	0.1010	***0.0820***	***0.0819***	***0.0837***	***0.0820***	***0.0820***	***0.0820***	***0.0820***
Mn	0.4305	0.0167	0.0165	0.0161	0.4135	0.0149	0.0129	0.0160
Al	0.0010	0.0030	0.0319	0.0064	0.0027	0.0020	0.0044	0.0029
Ti	0.0002	<DL	***0.0285***	0.0006	0.0003	<DL	0.0010	***0.0091***
Cr	9.2000	9.3160	9.3550	9.4850	9.3400	9.3530	9.4370	9.2930
W	1.0800	1.1480	1.1610	***1.4970***	1.1810	1.1630	1.1580	1.1330
N	0.0400	***0.0260***	***0.0154***	**0.0262**	0.0390	***0.0260***	***0.0190***	***0.0030***
V	0.1854	0.1890	0.2106	0.2111	0.1844	***0.0883***	***0.0032***	***0.1887***
Ta	0.1024	0.0980	0.1070	0.100	0.1100	0.1020	0.0930	0.1010

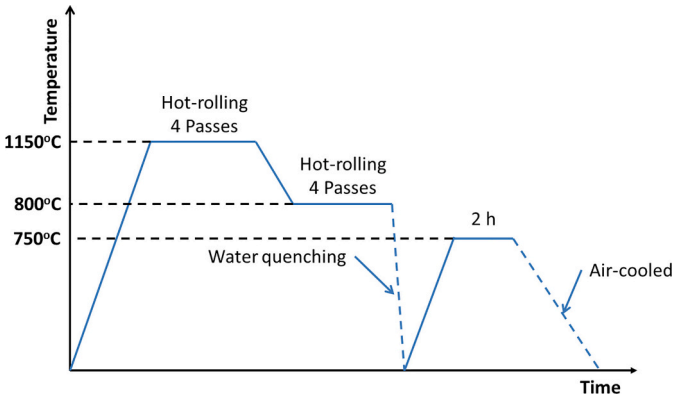

Fig. 1. Scheme of thermo-mechanical treatments applied to the Alloys.

temperatures. In order to increase the amount of MX precipitates in combination with refinements of the microstructure such as prior austenite grains, laths size, blocks, and packets. A successful demonstration of improved strength was achieved from appropriate TMTs application on FM steels [24–26]. Similar TMTs were applied on RAFM steels, showing sub-grain and precipitates refinement [27–29] with promising superior mechanical strength. X. Zhou et al. [30] review and disccus the strategies to obtain some specific microstructures for power and nuclera plants. Recently, alloy composition refinement is being explored by ORNL [31,32], developing the castable nanostructured alloys (CNAs) for increasing the amount of MX. The alloy chemistry was adjusted by adding N or Ti and modifying alloying elements to balance austenite stabilizers such as C, N, and Mn with ferrite stabilizers (Cr, W, Ta, V, Si, and Ti). The results show an increase in number density and refinement of MX.

In the framework of materials programme in Europe under the consortium, EUROFusion, alloy chemistry adjustment, and TMTs application are being performed in new advanced steels for structural components applications to improve the mechanical strength at high temperatures.

The aim of this work is to investigate the microstructural characteristics and precipitation behavior after tempering at 750 °C (size, number density, and nature) of eight new technological 9% Cr RAFMs, whose chemical compositions have been finely tuned and subsequently thermomechanical treated followed by tempering treatment in order to obtain a fine dispersion of $M_{23}C_6$ and MX homogeneously distributed in the matrix.

2. Experimental procedure

Eight advanced RAFM steels referred to as K465A, K468A, K473A, K476A, K466A, K469A, K471A, and K474A were produced and thermomechanical treated by OCAS (Belgium). Their chemical compositions, in weight percent (wt%), are given in Table 1. Taking as reference the composition of EUROFER97 [33] (Alloy K465A), the chemical composition on each alloy was finely tuned or was remained unchanged to evaluate the metallurgical properties. C content was reduced from 0.10 wt% (Alloy K465A) up to ~0.082 wt% on all others steels. Ta content (0.1 wt%) has remained constant in all the Alloys. C was the only alloying element tuned on Alloy K466A. N concentration was reduced up to 0.026 wt% on Alloys K468A, K476A, and K469A. On Alloy K473A Ti was added and N was reduced up to levels of 0.015 wt%. Alloy K471A is practically V free and Alloy K474A is N free with a small amount of Ti. Finally, on Alloy K476A the W content was increased from 1.1 to 1.5 wt %. Two thermomechanical treatments were applied sequentially to the eight alloys. The first one consists of four hot-rolling passes at 1150 °C, followed by cooling at 800 °C, at which temperature the alloys were subjected to other four passes and then water quenched (Fig. 1). After ausforming treatment, the materials were tempered at 750 °C for 2 h in a vacuum and then air cooled.

The microstructures of the Alloys have been characterized on thin foils and carbon extraction replicas on the cross-section with respect to the rolling direction. Transmission electron microscopy (TEM) and scanning transmission electron microscopy (STEM) were carried out on a JEOL JEM 3000F to study the microstructure after ausforming treatments and after tempering. The microscope is equipped with an Energy-dispersive X-ray spectroscopy (EDS) INCA microanalysis suite and a Gatan Enfina Electron Energy Loss Spectroscopy (EELS) spectrometer. The STEM unit has an annular dark field detector (ADF) that makes it possible to acquire both, low angle annular dark field (LAADF) or high angle annular dark field (HAADF) images by changing the camera length. The characterization of microstructure has been mainly performed in STEM mode by acquiring LAADF images or –in some cases- HAADF images to remove contrast from forest dislocations and to obtain a purer *Z*-contrast of the precipitates in the images. EELS spectrum images were acquired in STEM mode with a beam diameter of aprox. 0.5 nm and a convergence semiangle of 12 mrad. The EELS spectra collection semiangle was 18 mrad. The elemental maps and line profiles were extracted from the core loss edges by background substraction using a power law background and integrating over an energy window across the corresponding core loss edge. TEM discs with 3 mm of diameter were thinned using a Struers Tenupol-5 electropolishing unit with a methanol-sulfuric (4:1) solution at 10 V and at 15 °C. Microchemical analysis performed by EDS on secondary phases was carried out on carbon extraction replicas to avoid matrix effects. High-Resolution Transmission Electron Microscopy (HRTEM) was used to identify the secondary phases by means of digital diffraction pattern analysis. Lattice images of selected precipitates were taken along main zone axes and their corresponding digital diffraction patterns were calculated with Gatan Digital Micrograph® software. The patterns were indexed according to the structures of the precipitates present in the samples. In addition, Electron Energy Loss Spectroscopy (EELS) technique was used to determine if the MX and M_2X type precipitates are carbides, nitrides or carbo-nitrides. EELS analyses were performed on extracted residue obtained by anodic dissolution of the matrix. The secondary phases extracted were mounted on Lacey type grids. Only were analyzed precipitates located on the hole of the grids to avoid C contamination. Before to EELS acquisition, several analyses were performed in the

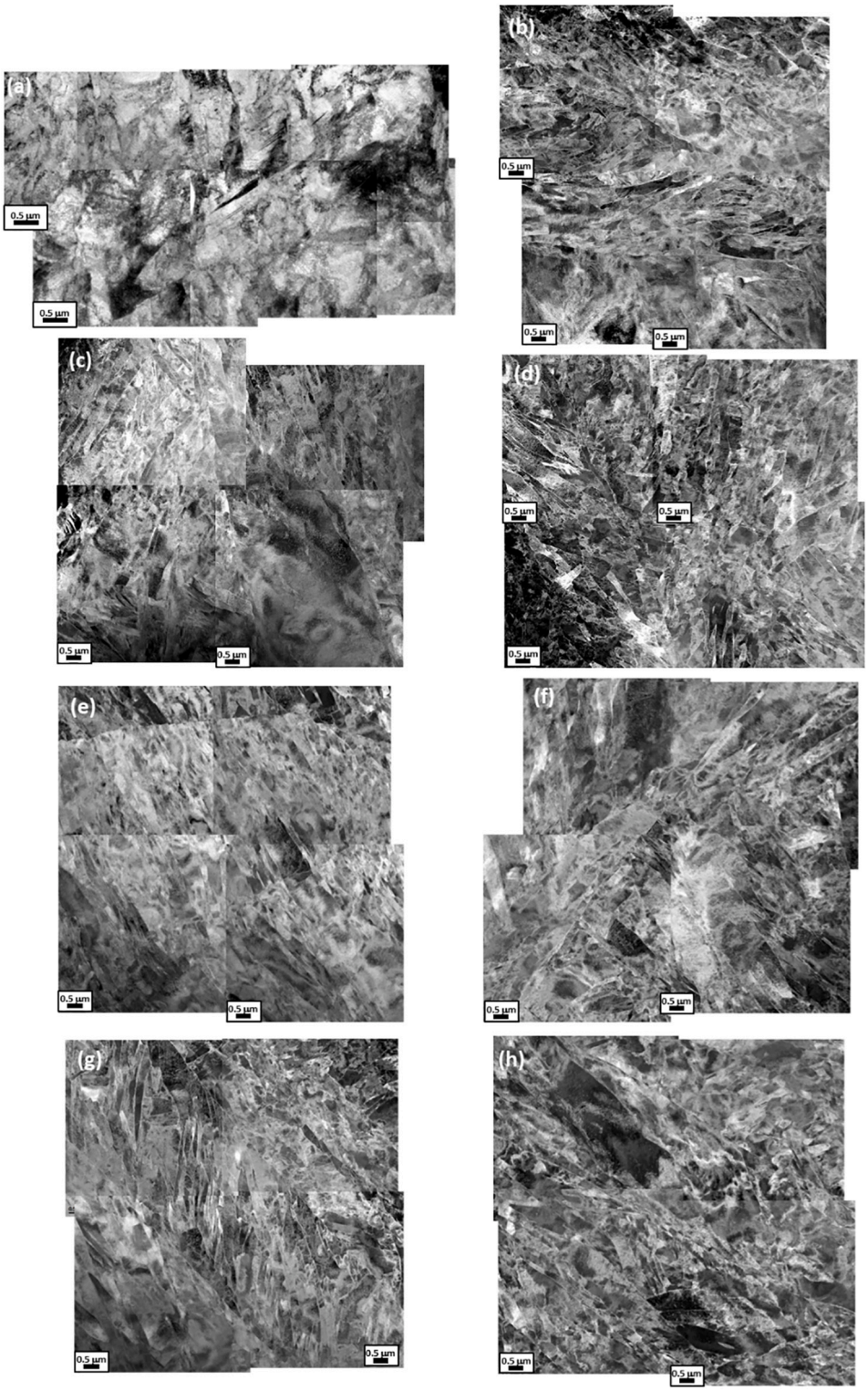

Fig. 2. LAADF-STEM images of the eight alloys after water quenching: a) Alloy K465A, b) Alloy K468A, c) Alloy K473A, d) Alloy K476A, e) Alloy K466A, f) Alloy K469A, g) Alloy K471A and h) Alloy K474A.

surrounding area of the precipitate to check a possible C contamination.

3. Results

3.1. Microstructure after water quenching

Fig. 2 shows the microstructure of the Alloys after water quenching. All the steels present un-tempered martensitic lath structure inside of elongated prior austenite grains. The dislocation density is extremely high due to the thermo-mechanical treatments applied. A detailed examination of the microstructure revealed that any of the materials present errite grains. However, the TEM investigations performed on the Alloys after water quenching did reveal the presence of a few primary precipitates within sub-grains of martensite laths, nucleated at

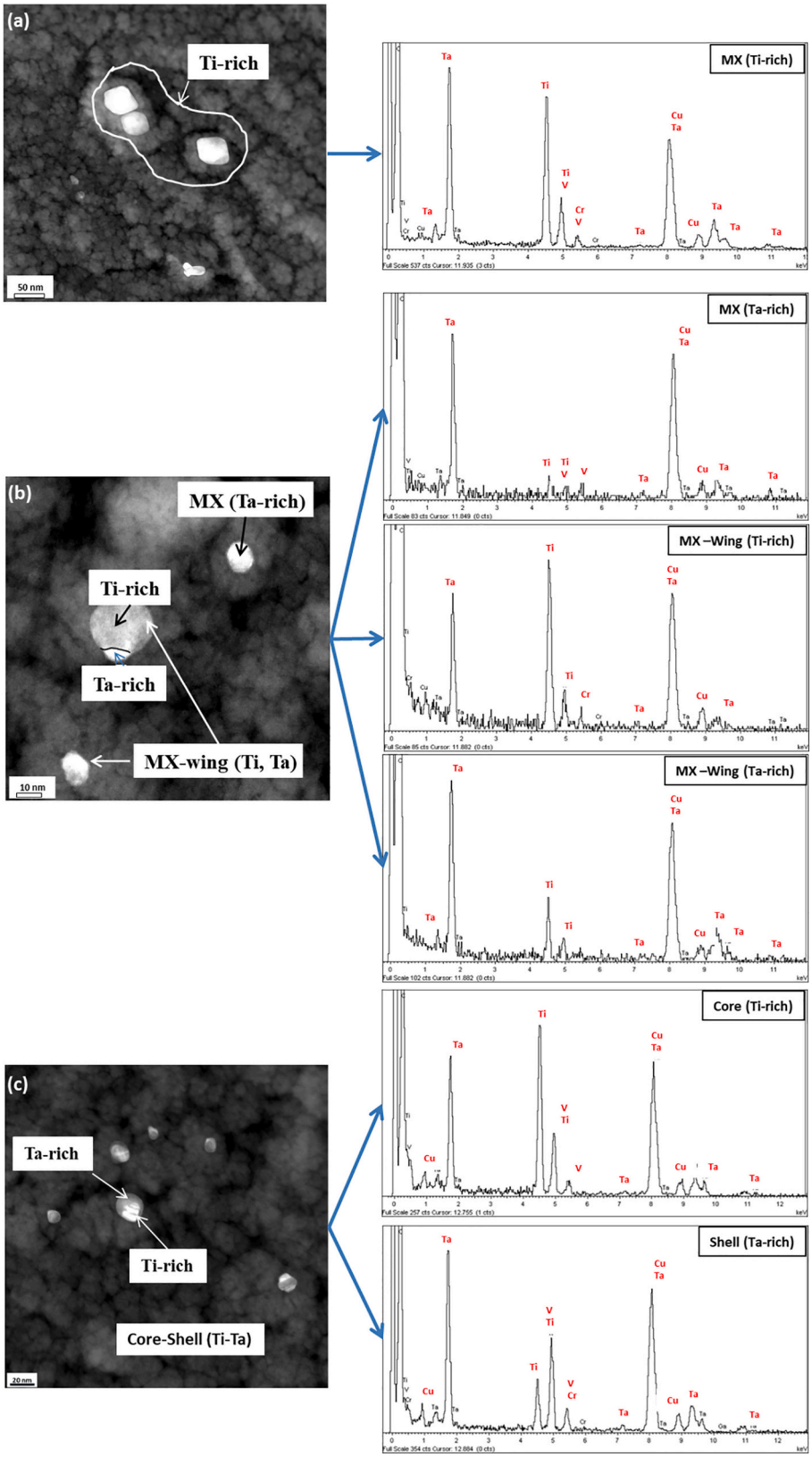

Fig. 3. STEM images of carbon extraction replicas and typical EDS analysis of the precipitates identified on Alloy K473A after water quenching: a) MX (Ti-rich) and b) MX (Ta-rich), MX-Wings and c) Core-Shell (Ti-Ta) precipitates.

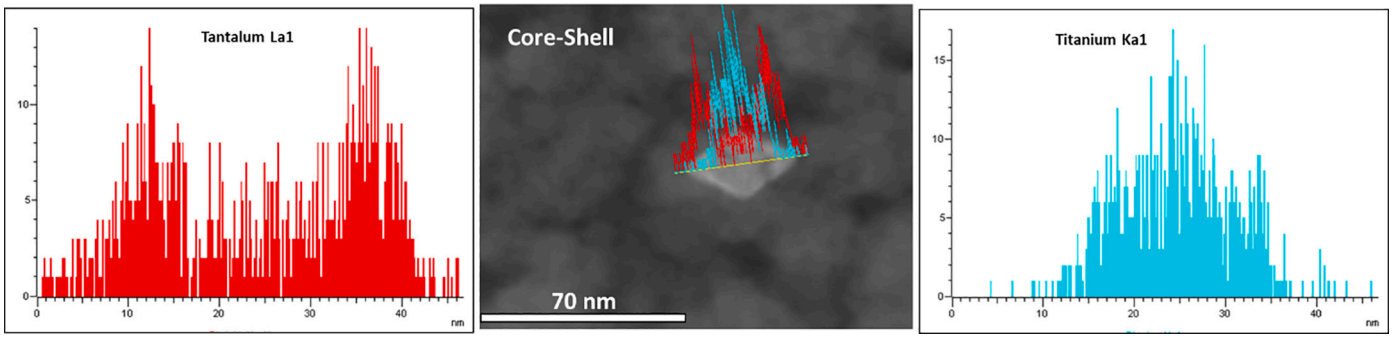

Fig. 4. EDS line scan on core-shell precipitates on Alloy K474A after water quenching.

dislocations.

Carbon extraction replicas were prepared in order to know the precipitate-type in this state. Several attempts were done in the eight alloys, but the precipitates only could be extracted on the Alloys K473A and K474A in which Ti was added. On Alloy K473A MX-Ti rich, MX-Ta rich, MX-wings (Ta, Ti) and core-shell phases (Ti-Ta or Ti-V) were identified (Fig. 3). Similar secondary phases were detected on Alloy K474A after ausforming, but in this steel, the core-shell precipitates were only of the type Ti-Ta (Fig. 4). The most abundant phase in both Alloys is MX-Ta rich.

In general, the size of Ti-rich and Ta-rich precipitates is finer on Alloy K474A than Alloy K473A, except on core-shell phases. MX-Ti rich particles on Alloy K474A exhibits a mean diameter between 4 and 6 nm versus Alloy K473A which sizes vary from 55 to 65 nm, principally attributed to the higher Ti content and its solubility, the explanation of which will be discussed later.In this Alloy, the mean diameter of MX-Ta rich and MX-wings is in the range from 15 to 25 nm, while in the Alloy K474A the size of MX-Ta rich and MX-wings varies from 4.5 nm to 27 nm. In contrast, the size of the core-shell phases is finer on Alloy K473A (15 to 25 nm) than the Alloy K474A (20 and 40 nm). In addition, isolated Ti-wings particles of approximately 80 nm on Alloy K474A were observed not only on carbon extraction replicas but also on extracted residue for EELS analysis.

3.2. *Microstructure after tempering at 750 °C for 2 h*

The microstructure of the eight Alloys after tempering at 750 °C/2 h is shown in Figs. 5 and 6. Tempering has produced dislocation recovery and significant precipitation of secondary phases. On Alloys K465A (Fig. 5b) and K473A (Fig. 5h), the sub-grains within the martensite laths start or had developed into fairly equiaxed grains with little trace of the original lath-martensite structure. In general, the distribution of secondary phases is quite homogeneous, except in the Alloys K468A (Fig. 5e–f) and K469A (Fig. 6e–f), which present areas with a different population of precipitates. On Alloy K468A some particle coalescence was observed in areas with a high density of precipitates. Coarser phases are mainly precipitated at austenite and lath boundaries, while finer particles are preferentially located at lath and sub-grain boundaries and also inside of martensite laths.

The identification and the chemical composition of each kind of precipitate were performed on carbon extraction replica to avoid matrix effect. $M_{23}C_6$ and MX were the only two types of precipitates identified by means of EDS spectra and digital electron diffraction pattern analysis on Alloys K465A, K468A, K473A, and K476A (Fig. 7a–d), while in the Alloys K466A, K469A, and K471A apart of $M_{23}C_6$ and MX, M_2X were identified (Fig. 7e–l). Tempering at 750 °C/2 h provides M_2X instead of MX on K466A and K469A. Only a few M_2X-type precipitates were detected on Alloy K471A; the most abundant being of MX-type.

All the precipitates labeled in Fig. 7 were analyzed by EDS. Fig. 8 (a–c) shows an example of the typical EDS spectra taken from different types of precipitates corresponds to Alloy K466A. $M_{23}C_6$ and M_2X can be clearly distinguishable from EDS spectra comparing the peak heights (I) of Cr and Fe and setting its relation shape. $M_{23}C_6$ exhibits Cr/Fe ratios around 2.4, while the M_2X has ratios of approximately 19.

The micro-chemistry of the secondary phases identified on each Alloy is showed in Table 2. In this table, it can be observed that MX-Ta rich were not detected on carbon extraction replica on Alloys K465A and K476A. Although this phase was not observed, that not means that this kind of precipitate is not present. Probably their size is lower than 3 nm and they could not be extracted on carbon replicas, and/or the amount is very low. In fact, these particles were detected and analyzed by EELS, but its density is low in comparison with the M_2X and MX-V rich.

The crystal structure of precipitates was identified based on the analysis of digital diffraction patterns (Fig. 8 g–i). The lattice parameter of $M_{23}C_6$ (Face Centered Cubic, FCC) was determined to be in the range between 10.6 and 10.8 Å, values in good agreement with the reported in Refs [34,35]. The lattice parameter of V rich MX (FCC) was in the range of 4.08 and 4.15 Å, values close to that of VC and VN reported, 4.139 Å and 4.15 Å [36,37]. The MX-Ta rich precipitates of the present study exhibit lattice parameters about 4.35 Å, this value is very close to the lattice parameter of TaN (4.33 Å) and TaC (4.45 Å) [38]. M_2X presents Hexagonal Close Packing (HCP) structure with the lattice parameters a = b = 2.75 Å and c = 4.44 Å, according to Cr_2N HCP structure [34].

Statistics analysis of size (particle diameter) and number density was determined on carbon extraction replica on the area of $\sim 1.20.10^{-10}$ m^2 (Table 3). The Alloy with the highest density of particles is the Alloy K473A, probably due to the Ti addition, which has led to the formation of titanium-rich precipitates apart from $M_{23}C_6$ and MX rich in V and/or Ta. From Table 3, it is clear that there are no significant differences in the range of sizes for each kind of precipitate. M_2X exhibits coarser sizes than MX. Alloys K465A, K466A and K469A present a higher number of M_2X than MX. However, the density of M_2X on Alloy K471A is lower than MX. As can be seen in Table 3, the Alloy K465A (reference material) which contains the higher C, and N concentrations exhibit thickened M_2X and MX precipitates. As can be seen in Table 3, the upper size measured of MX on Alloy K476A is 60 nm. Nevertheless, it is important to remark that only a few V-rich particles present this size.

The size distribution and relative frequency of the secondary phases are shown in Fig. 9. The statistical results have been grouped into two graphs depending on the kind of precipitates. The size and frequency of

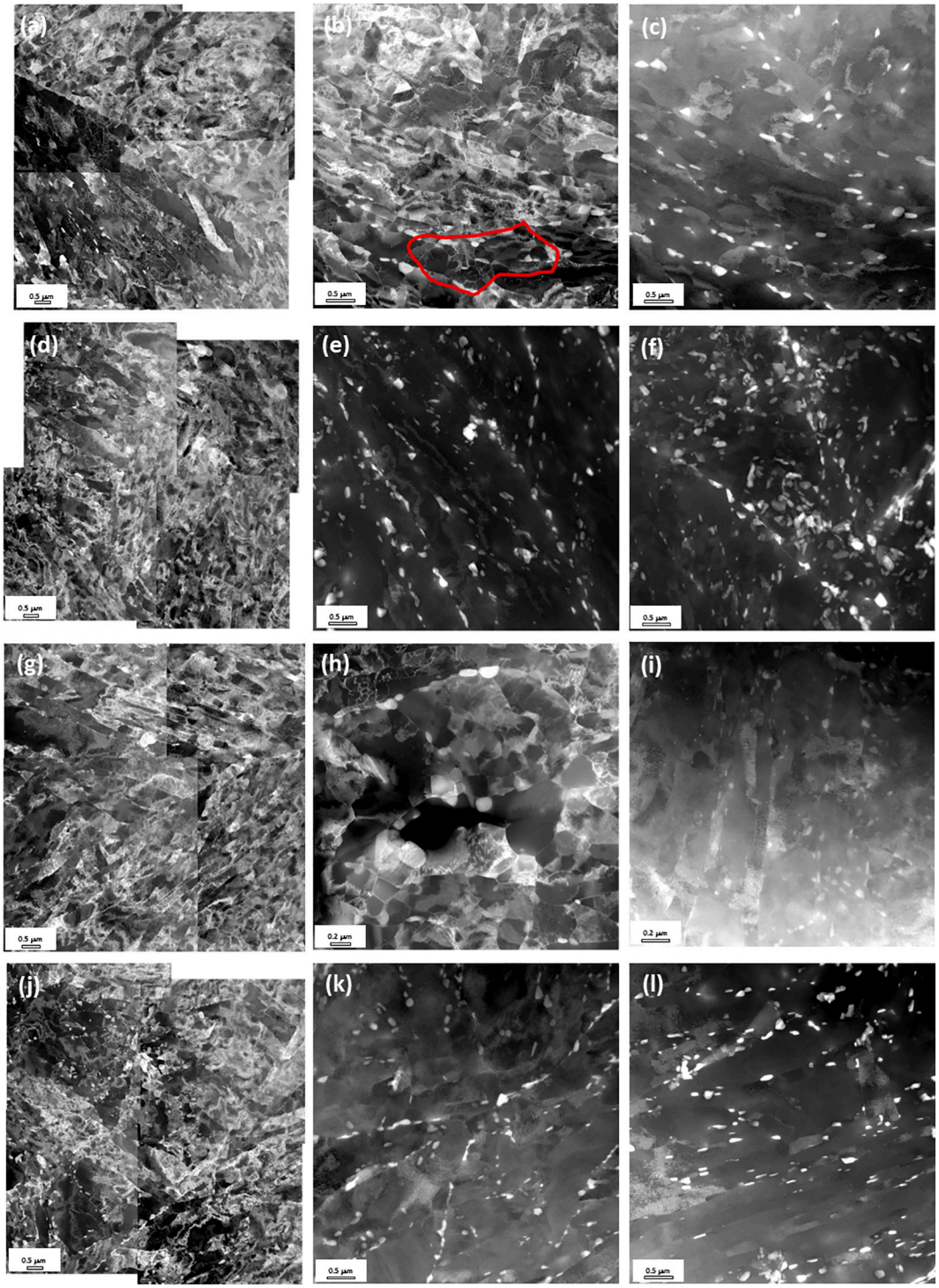

Fig. 5. STEM (LAADF and HAADF) images of the alloys after tempering treatment: a–c) Alloy K465A, d–f) Alloy K468A, g–i) Alloy K473A and j–l) Alloy K476A.

the alloys that present $M_{23}C_6$-type carbides and MX are plotted in the graph a), while the alloys which contain besides M_2X precipitates are represented on graph b). It is observed that the Alloy K468A exhibits the highest percentage (~30%) of fine MX precipitates with sizes between 3 and 10 nm. Taken as a reference that the highest size of MX precipitates is 50 nm since the number of this kind of particles with larger sizes is very low, it is clearly deducible from Fig. 9a that the Alloys with Ti added in its composition (K473A and K474A) lead to an increase in the number of MX particles, being higher on Alloy K473A than in the Alloy K474A.

Comparing Fig. 9a and b can be observed the significant reduction of the percentage of fine precipitates (<10 nm) when M_2X are nucleated together with MX particles. This behavior can be attributable to the reduction of N and/or V content on Alloys K466A, K469A, and K471A. For this reason, it is to be expected that the Alloy K465A exhibit the greatest amount of MX and M_2X. However, the results seem to indicate that high N contents (0.04 wt%) on materials with the thermomechanical and tempering treatments described in this work, it is favored the coarsening instead of nucleation.

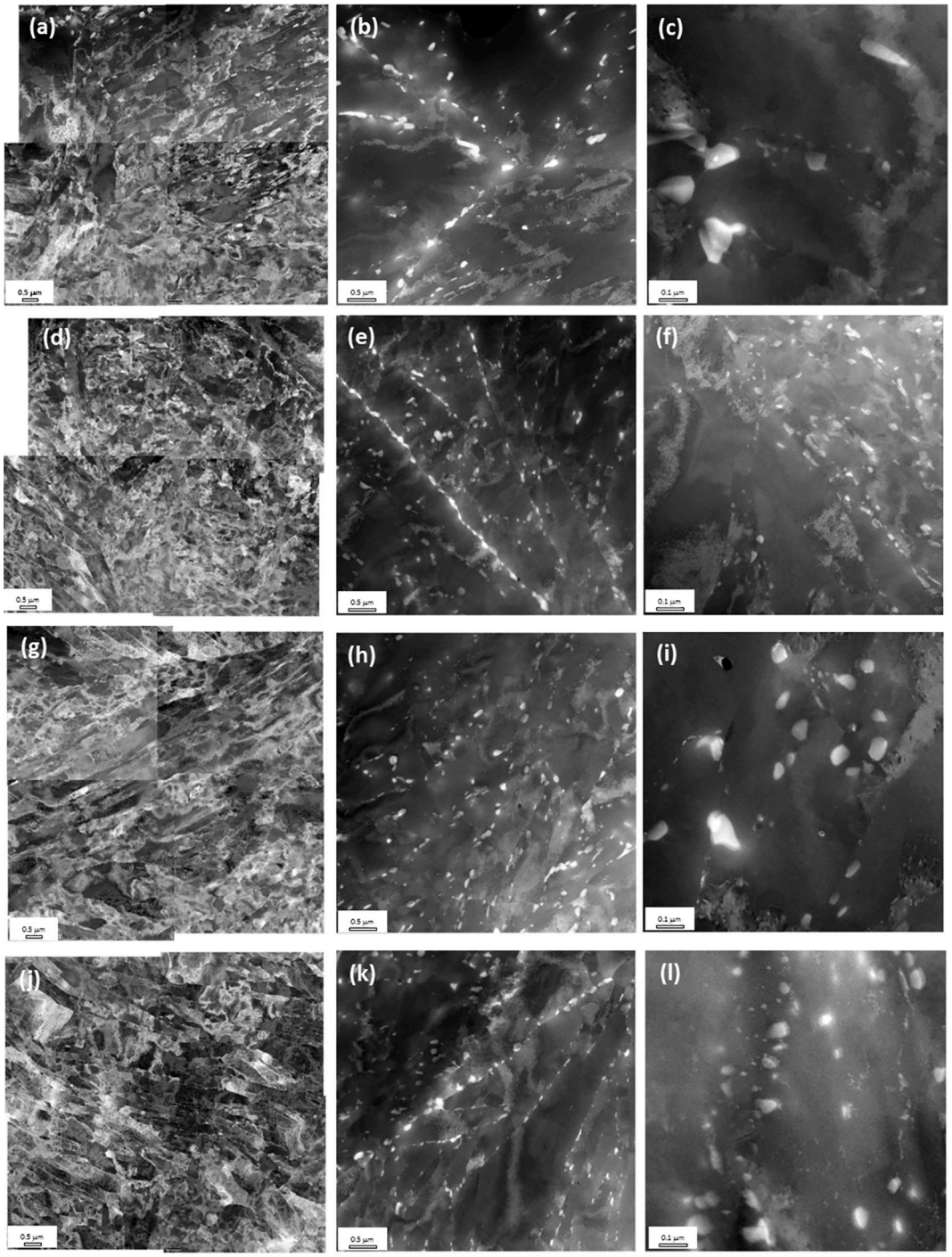

Fig. 6. STEM micrographs of the alloys after tempering treatment: a–c) Alloy K466A, d–f) Alloy K469A, g–i) Alloy K471A and j–l) Alloy 474A.

3.3. Carbon and nitrogen contents on precipitates

EELS analysis have been performed on M_2X and MX (Ta, Ti and V rich) particles to know if these precipitates are carbides, nitrides and/or carbo-nitrides. According to the methodology described in Section 2, line scan, static beam, and mapping modes were acquired on each Alloy. The EELS acquisition was performed mainly in the range of energies from 200 to 1500 eV. An additional spectrum on MX-Ta rich precipitates was acquired in the range from 1000 to 2500 eV to detect the Ta. Relative quantification has been done in order to obtain a first estimation of the C/N and N/C ratios on each kind of secondary phase. All the M_2X (Fig. 10) analyzed independently of the Alloy (K465A, K466A, K469A, and K471A) are carbo-nitrides, with higher N content than C. The N/C ratio on these particles varying between 1.5 and 3.

Concerning the MX-V rich particles (Fig. 11), the scenario is more complex (Table 4). According to EDS analysis performed on carbon extraction replicas, this phase is present on five (K465A, K468A, K473A, K476A, and K466A) of the eight alloys investigated in this work (see Table 2). In Alloy K465A the majority of the V-rich particles are pure V-nitrides (VN), although a very few V(C, N) with N/C ratios of ~3–4 were analyzed. A few pure VN was also found on Alloy K476A, but in this material, the great percentage are V (C, N). All the V-rich precipitates analyzed on Alloy K466A showed to be V carbo-nitride (N/C ~ 4). In contrast, the Alloy K468A contains V(C, N) with similar ratios to the

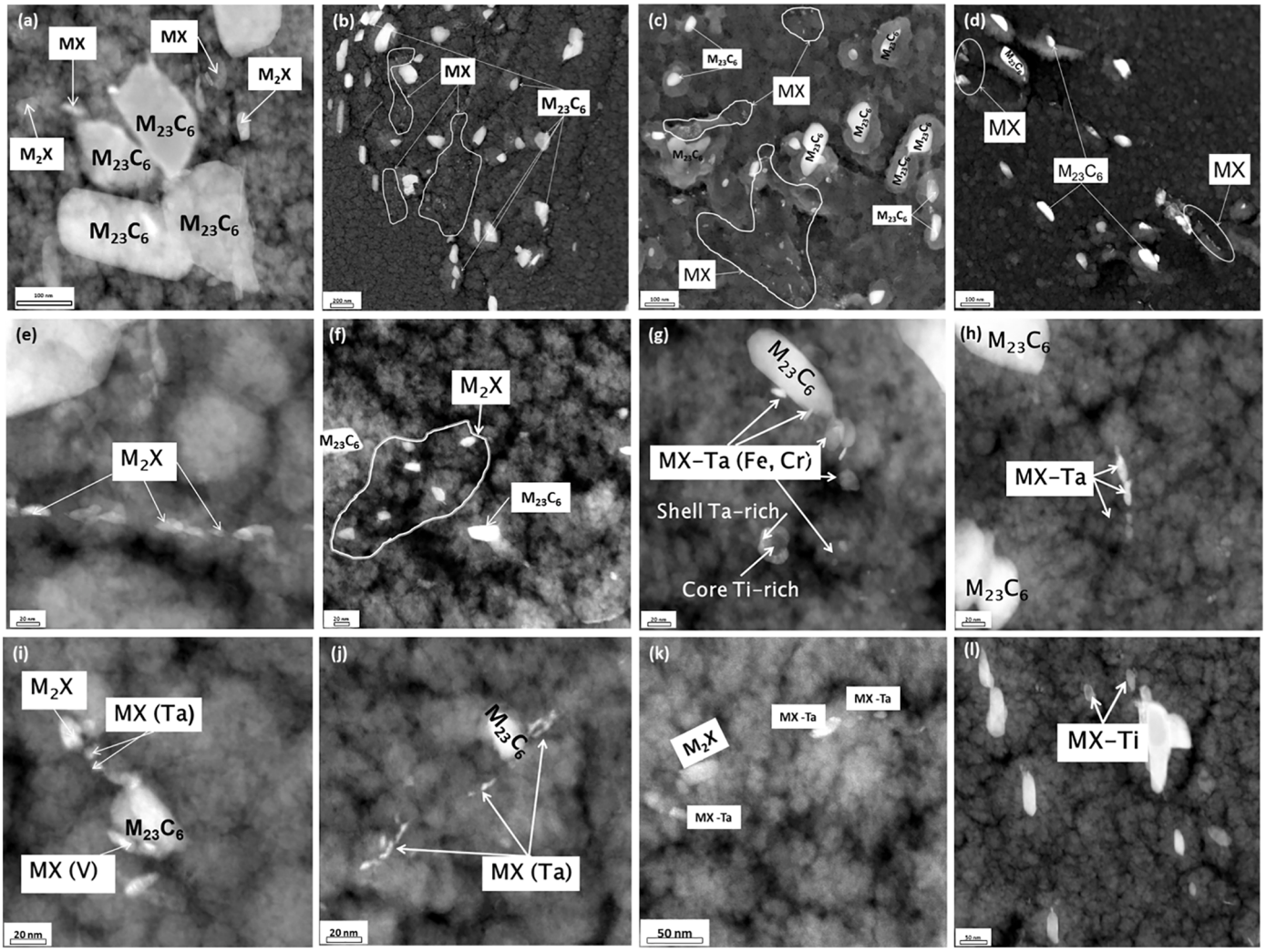

Fig. 7. STEM micrographs of carbon extraction replicas after tempering at 750 °C/2 h: a) Alloy K465A, b) Alloy K468A, c) Alloy K473A, d) Alloy K476A, e–i) Alloy K466A, f–j) Alloy K469A, g–k) Alloy K471A, and h–l) Alloy K474A.

Alloys K465A and K466A in conjunction with carbo-nitrides with high N/C ratios (~6–8), as can be seen in Table 4.

All the MX-Ta rich precipitates are mainly carbo-nitrides (Table 4). Only a very few TaC particles were analyzed on Alloy K465A (Table 4). Fig. 12 shows representative micrographs and EELS analysis of this kind of precipitates. The qualitative atomic percentage of N measured by EELS is higher than the C content on Alloys K465A, K468A, and K476A, which ratios are indicated in Table 4. As can be seen in this table, Alloy K465A exhibit only Ta-rich precipitates with higher N than C, attributable to its high N content (0.04 wt%). the Ta-rich particles on Alloys K468A and K476A clearly exhibit two N/C ratios (lower ~2 and higher ~5 values), while in the alloy K469A, the N/C ratio (~1.5–2) is close to the lower ratio of the Alloys K468A, K474A, and K476A. Only in the Alloys K466 and K471A were found Ta carbo-nitrides with higher C than N, presenting both steels similar C/N ratios ~1–2.

Two kinds of secondary phases rich in Ti were identified by EDS on Alloys K473A and K474A after tempering on carbon extraction replicas; MX-Ti rich and core-shell precipitates. Representative EELS analysis of these particles is shown in Fig. 13. As can be seen in Table 4, the precipitates rich in Ti are carbo-nitrides with higher N than C, independently if they are Ti (C, N) or core-shell. Concerning to the core-shell phases, both Alloys present similar N/C ratio in the core, approximately 2. The V shell on Ti-rich precipitates contains higher N than C. However, the Ta shell is richer in C than in N.

4. Discussion

Development of structural material for fusion energy is being guided by the operational conditions expected in future power plants, and by lifetime and safety requirements associated with economics and environmental issues. To achieve high thermodynamic efficiency is necessary to increase the operational conditions and consequently is required the use of structural materials with high strength at high temperatures. The basic methods of strengthening steels at elevated temperatures are solute hardening, precipitation hardening, dislocation hardening, and boundary and/or sub-boundary hardening [40,41]. The addition of alloying elements such as Mo and W, which have larger atomic sizes than the Fe solvent atoms, favored the hardening of solid solution. On the other hand, to increase the hardness by secondary precipitation, elements such as N, V, Ta, and Ti are usually added to form fine

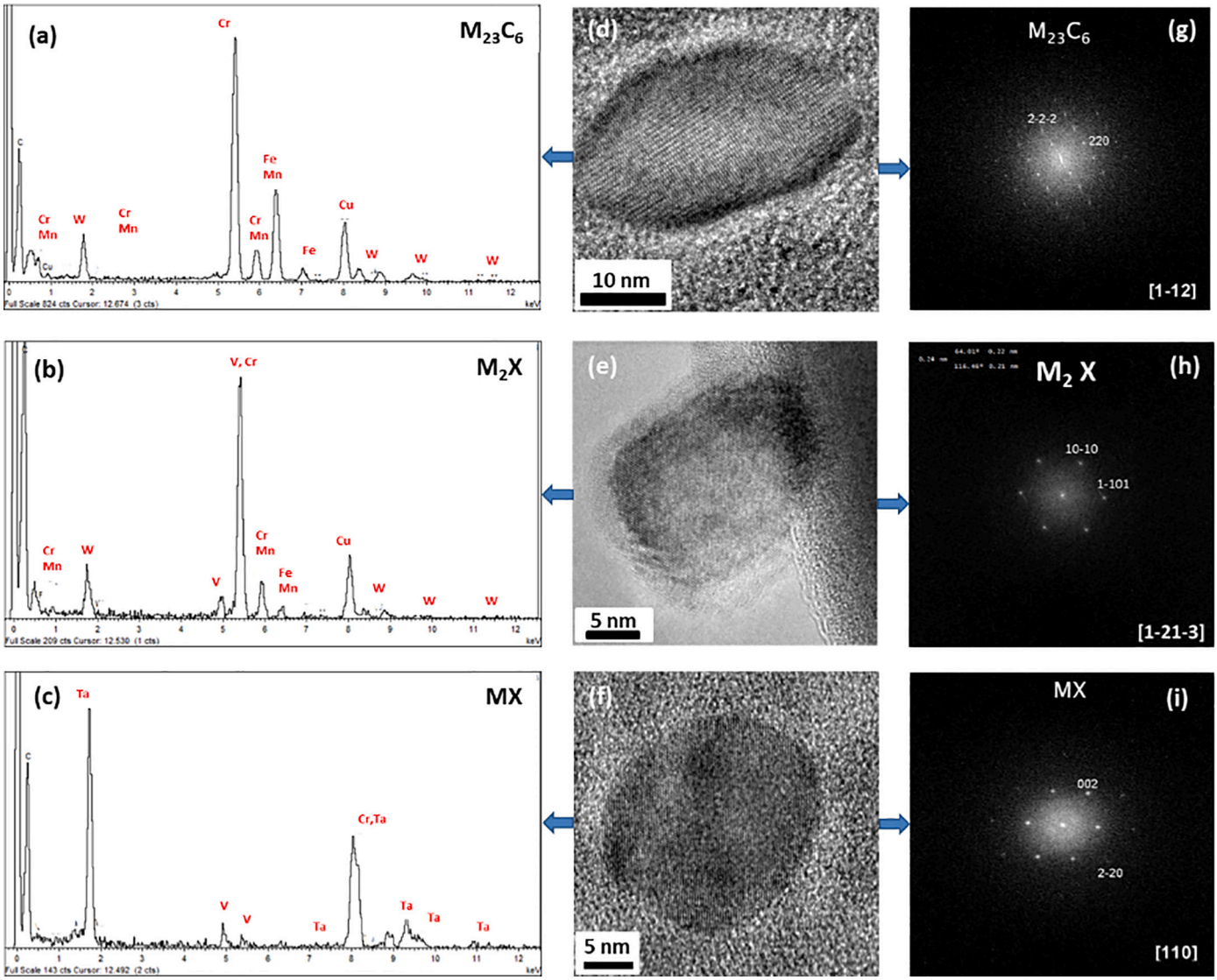

Fig. 8. Representative HRTEM of the three types of precipitates (d–f) identified after tempering; (a–c) Typical EDS spectra and (g–i) digital diffraction pattern.

intermetallic compounds ($M_{23}C_6$, M_2X, MX, etc) dispersed through the matrix and at the grain and sub-grain boundaries. The dispersion of fine precipitates stabilizes free dislocations and the subgrain structure against recovery, which further enhances dislocation hardening and sub-boundary hardening, respectively. With this objective, different alloy compositions were designed in order to promote the formation of larger amounts of fine MX and to reduce the size of $M_{23}C_6$, so these carbides coarse during aging or creep allowing at the same time extensive coarsening of the martensite laths and consequently loss of strength.

In order to evaluate if C content reduction would produce a decrease of $M_{23}C_6$ size, C content was reduced on seven of the eight Alloys investigated (Table 1), based on the chemical composition of EUROFER97 (Alloy K465A). C was the only element tunned on Alloy K466A. Comparing the size and the percentage of the secondary phases on Alloys K465A and K466A (Fig. 9), and taking as reference that the lower size of $M_{23}C_6$ is 50 nm because Alloy K465A presents MX and M_2X with sizes of 50 nm (Table 4), it is deducible that the Alloy K466A exhibits a higher number of fine Cr-carbides with sizes between 70 and 160 nm than the Alloy K465A. Nevertheless, the relative frequency of $M_{23}C_6$ in the range from 50 to 350 nm is a little bit different between both Alloys; 78% for Alloy K465A and 74% for Alloy K466A. These values seem to suggest that the C reduction seems to be effective to reduce the size and the amount of $M_{23}C_6$. Our results are in concordance with the work performed by F. Abe et al. [42], who proved the effectiveness to reduce the amount of $M_{23}C_6$ Cr-rich decreasing carbon concentration.

Ti was added on Alloys K473A and K474A (Table 1) in order to obtain more stable precipitates to maintain the effect of precipitation strengthening as long as possible. It is well known that the solubility of Ti on steels is very low even at normalizing temperature, and hence precipitation of fine Ti-carbonitride after tempering is very difficult. The difference in size of the Ti MX observed in the K747A and K473A Alloys seems to suggest that an increase in the Ti content, with the thermo-mechanical treatments applied, together with its low solubility have not been sufficient to obtain a homogeneous distribution of this alloy, and consequently the growth process has been favored over the nucleation process. Further more, we have observed Ti-rich precipitates with different morphologies after TMT which means that MX-Ti rich remained without dissolving at 1150 °C (Fig. 1). After tempering at 750 °C/2 h, it was not observed further Ti-particles precipitation. M. Taineke et al. [43] observed that all the MX-Ti rich particles dissolve at temperatures above ~1230 °C when N is not added to steel and reprecipitate after tempering. However, when the steel contains nitrogen, the added Ti precipitated as titanium carbo-nitride, but with higher N than C, even when the N content is very low (0. 0030 wt%, Alloy K474A). Consequently, MX-Ti rich precipitates have remained in the steel after four passes at 1150 °C. According to the results presented by Taineke

Table 2
Chemical composition (at. %) of phases identified after tempering at 750ºC/2 h on the Advanced RAFM steels studied.

Alloy	Fe	Cr	W	V	Ta	Ti	Mn	Phase
K465A	29.25 ± 2.06	65.00 ± 2.70	2.60 ± 0.63	1.15 ± 1.30*	0.40 ± 0.13*		2.13 ± 1.00	$M_{23}C_6$
	3.50 ± 1.54	80.17 ± 3.50	2.00 ± 0.75	11.10 ± 5.14	1.44 ± 0.36*		3.18 ± 2.28*	M_2X
	2.70 ± 1.60*	16.30 ± 4.40	2.00 ± 1.10*	64.50 ± 6.00	14.16 ± 4.05		1.60 ± 1.30*	MX-V rich
K468A	28.32 ± 1,85	65.84 ± 1.50	3.10 ± 0.58	0.64 ± 0.47*	0.68 ± 0.30		1.70 ± 0.62	$M_{23}C_6$
	2.66 ± 2.10	11.07 ± 3.06	7.92 ± 4.90	28.92 ± 9.9	49.27 ± 8.32		2.58 ± 1.92	MX-Ta rich
	2.50 ± 1.24	16.86 ± 6.25	4.52 ± 3.60	52.37 ± 9.90	25.46 ± 7.50			MX-V rich
K473A	25.68 ± 2.84	63.33 ± 4.21	6.03 ± 2.12	0.32 ± 0.20*	6.30 ± 4.63*	0.40 ± 0.31*		$M_{23}C_6$
	1.08 ± 0.72	4.64 ± 1.9	–	12.90 ± 8.50	23.14 ± 5.40	58.50 ± 12.19		MX–Ti-rich
	1.34 ± 1.30	6.01 ± 0.84	–	20.13 ± 6.91	71.18 ± 8.35			MX-Ta rich
	1.49	10.17		61.31	26.56	0.47		MX-V rich (1 analysis)
K476A	28.40 ± 5,10	64,00 ± 2,01	4.00 ± 1.65	1.62 ± 2.14*	1.83 ± 1,7*	2.35 ± 0.55*	6.00 ± 0.06*	$M_{23}C_6$
	2.78 ± 1.74	17.95 ± 5.41	3.70 ± 2.44*	59.34 ± 11.63	15.88 ± 5.32	2.00 ± 1.40		MX-V rich
K466A	28.50 ± 2.01	65.47 ± 1.65	3.24 ± 0.66				2.34 ± 0.72	$M_{23}C_6$
	4.00 ± 1.38	83.85 ± 3.21	3.25 ± 0.94	6.30 ± 1.44			3.30 ± 1.38	M_2X
	2.61 ± 0.31	19.90 ± 3.72		49.04 ± 2.27	27.77 ± 5.94		1.55 ± 2.20	MX-V rich
	0.16 (1 analysis)	4.19 ± 1.74		26.81 ± 14.38	66.10 ± 14.97		2.81 ± 2.23	MX-Ta rich
K469A	27.35 ± 3.21	64.60 ± 1.07	1.77 ± 1.04	1.95 ± 1.28	–		1.43 ± 1.11	$M_{23}C_6$
	5.00 ± 1.50	87.50 ± 3.80	2.82 ± 1.15*	3.00 ± 1.74	6.60 ± 5.04*			M_2X
	2.55 ± 1.59	19.34 ± 3.12	–	18.61 ± 3.27	59.48 ± 5.36			MX-Ta
K471A	29.79 ± 1.72	67.67 ± 1.58	2.71 ± 0.41	0.11 (1 analysis)				$M_{23}C_6$
	6.36 ± 4.56*	16.70 ± 5.80			80.20 ± 6.50			MX-Ta rich
	6.00 ± 1.47	81.47 ± 8.35	1.85 ± 1.11	0.50 ± 0.20	10.34 ± 7.04		4.10 ± 1.17	M_2X
K474A	28.48 ± 2.27	68.46 ± 2.34	2.27 ± 0.74	0.80 ± 0.35				$M_{23}C_6$
	3.04 ± 2.73*	16.96 ± 5.85		20.00 ± 6.87	59.14 ± 7.86	16.18 (1)		MX-Ta rich
	1.60 ± 1.62*	6.59 ± 3.00		7.28 ± 5.02	18.71 ± 11.11	66.07 ± 13.40		MX-Ti rich

* Not present in all analysis.

Table 3
Number density and range of particle size diameter of the secondary phases identified after tempering at 750 °C/2 h.

Material	Number density (particles/m^2)	$M_{23}C_6$ (diameter nm)	MX (Ta or V rich) (diameter nm)	MX-Ti rich (diameter nm)	M_2X (diameter nm)
K465A	$5.1.10^{12}$	40–350 nm	8–50 nm	–	30–50 nm
K468A	$3.7.\ 10^{12}$	50–300 nm	3–20 nm		
K473A	$1.3.10^{13}$	50–350 nm	5–25 nm	MX-Ti; 55–65 nm Core-Shell; 20–40 nm	
K476A	$6.6.10^{12}$	50–350 nm	5–60 nm		
K466A	3.910^{12}	30–350 nm	5–20 nm		15–30 nm
K469A	3.210^{12}	30–350 nm	3–20 nm		15–30 nm
K471A	$6.1.10^{12}$	30–350 nm	3–20 nm		15–30 nm
K474A	$5.4.10^{12}$	30–350 nm	3–27 nm	MX-Ti; 20–40 nm Core-Shell; 20–40 nm	

and the described in this work, it seems clear that Ti addition on steels require higher temperatures of solubilization to enhance fine Ti carbonitrides during tempering.

Other relevant findings from the TEM investigations concern to M_2X carbo-nitrides. The precipitation behavior of this phase during tempering without ausforming on 9% Cr alloys has been less reported. For 12% Cr steels, the formation of M_2X depends on tempering temperature and it should be considered that precipitation occurs at temperatures lower than about 700 °C [44]. However, taking into account that the Cr content, the tempering temperature and the thermomechanical treatment is the same for the eighth alloys investigated in this work, the precipitation of M_2X seem also to be strongly influenced by the N and V concentration and the thermomechanical process applied

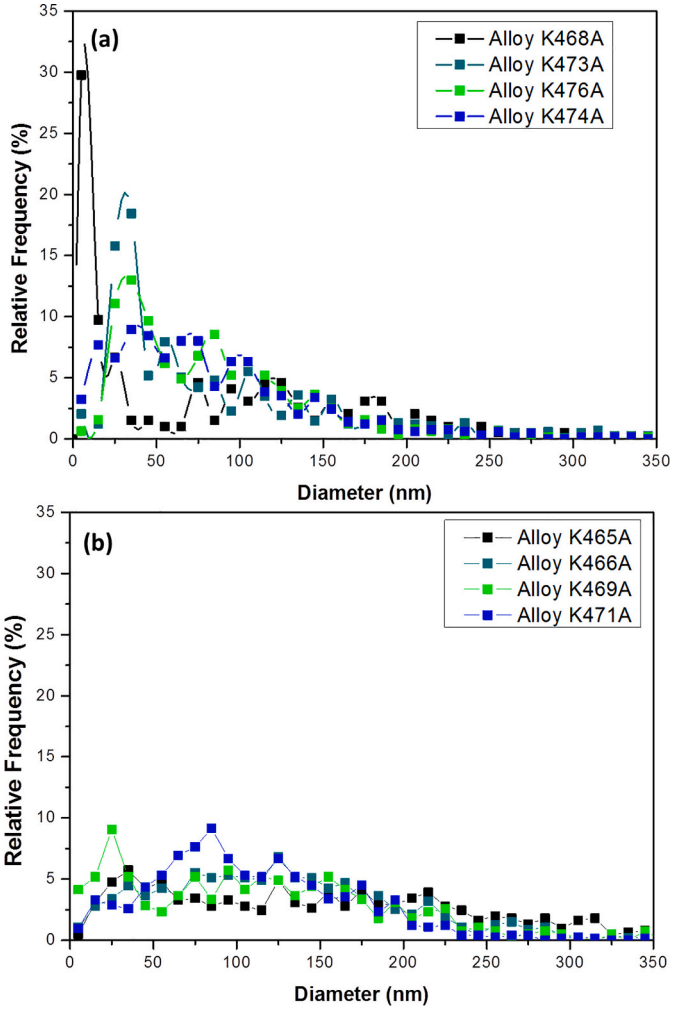

Fig. 9. Size distribution of secondary phases identified after tempering at 750 °C/2 h.

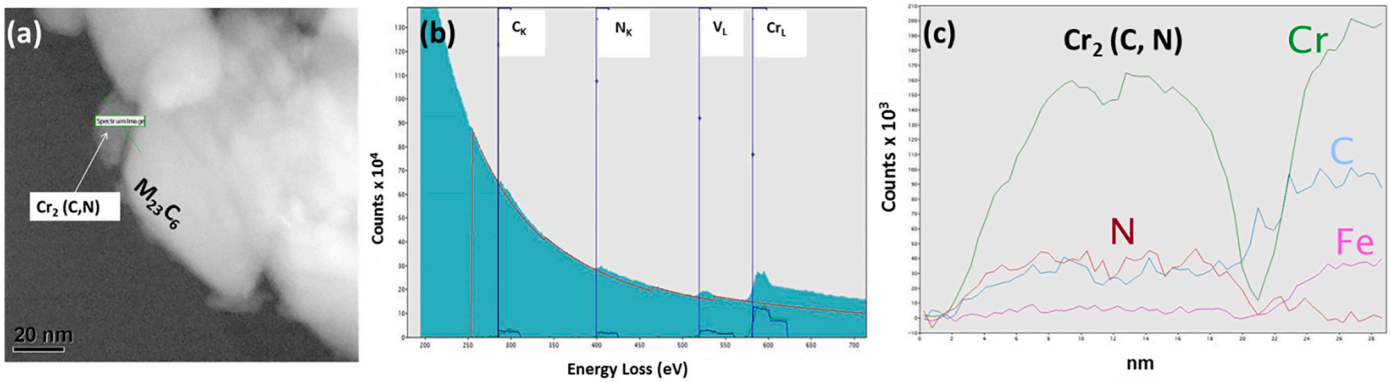

Fig. 10. Representative EELS analysis of the Cr-rich carbo-nitrides ($Cr_2(C, N)$) precipitated after tempering at 750 °C/2 h on Alloy K469A. (a) HAADF image of the extracted particles; (b) EELS spectrum, and (c) EELS line-scan.

in this work. We have detected M_2X particles after tempering on four alloys (K465A, K466, K469A, and K471A). The results obtained in this investigation suggest that N contents of 0.04 and 0.03 wt% (Alloys K465A and K466A, respectively) with V concentrations of approximately 0.2 wt% enhance M_2X precipitation instead of MX. In addition, it should be noted that this phase also precipitate when V content is lower than 0.2 wt% with N contents ≥0.2 wt% (Alloys K469A and K471A). The EELS results has shown that the M_2X is carbo-nitride containing higher N than C, with ratios N/C of approximately between 1.5 and 3. This phase has also been identified in similar advanced alloys which chemical composition has been finely tuned and thermomechanical treated to promote fine MX particles [45] or in the improved version of 9% Cr EUROFER97 alloy, whose normalization temperature was increased from 980 °C to 1150 °C with the purpose to bring most precipitates into the solution and therefore to create a better supersaturation [47]. The beneficial or detrimental effect of M_2X precipitates during long-time at high temperature under stress (creep) has not yet been entirely clarified. This phase could contribute to the precipitation of *Z*-phase in the form of Cr (Ta, V)N, and consequently, the creep strength would be significantly reduced [48,49]. K. Sawada et al. [50] investigate the effects of M_2X and MX on Z-phase formation during creep in 9Cr1MoVNb steel tempered at low and high temperatures, which results shown that M_2X forms after tempering at high temperatures (730°, 780 °C). However, the transformation of this phase during creep depends of tempering temperature. The M_2X particles disappear during creep with formation of MX when the steel is tempered at 680 °C and the creep rupture is delayed. In contrast, Z-phase formation was observed on creep samples tempered at 730° and 780 °C.

MX-V rich were not detected in neither carbon replicas (Table 2) nor in the phase extraction analyzed by EELS on Alloys K469A, K471A and, K474A. Taking in mind the spectra of the N and V contents designed, it could be concluded that the formation of V-rich particles during tempering at 750 °C for 2 h to be enhanced with V contents around 0.2 wt% and N concentrations in the range from 0.015 to 0.026 wt%.

It should be noted that often in the literature Ta-rich MX is referred as TaC and V-rich as VN, probably due to the crystal lattice parameter is coincident with the structure of these phases. However, no study has been published yet concerning the clarification of the nature (carbide, nitride or carbo-nitride) of the MX. The EELS analysis performed in this work suggests that the MX are predominantly carbo-nitrides. Only pure VN was detected on Alloy K465A and Alloy K468A. It is important to remark that the N/C and C/N ratios is a first approach to quantify the N and C content on MX. A general rule can not be established because the N/C and C/N ratios depend not only the N, V and or Ta content N contents, but also in these ratios has a strong influence the presence of the other phases such as the M_2X. When M_2X is present in one Alloy (K465A and K466A) and the N content is the highest (0.04 wt%) the N content in the V-rich MX is about 4 times higher than C. But nevertheless when M_2X is not present the N content on VX is higher than 5 times. In contrast, the scenario is very different in the Alloy K473A. The results of EELS analysis in this Alloy suggest that the N/C ratio (Table 4) is very similar in all the MX, independently if the particles are V, Ta or V-rich.

Regarding to Ta-rich MX only the Alloys K471A and K474A exhibit Ta carbo-nitrides with higher C than N with ratios C/N between 1.5 and 2. On Alloy K471A the N concentration is 0.2 wt% and also present M_2X, which it consumes practically all the N available in a solid solution and consequently, probably there is not N free to can to form Ta-rich precipitates with more N than C. Similar reason can be attributed for Alloy K474A, but because of the presence of Ti carbo-nitrides.

The experimental results obtained in this work indicate that the combination of thermomechanical treatments with chemical composition optimization can be devised to produce a homogeneous dispersion of fine and stable secondary phases to delay the microstructural evolution during operation at high temperatures.

5. Conclusions

The microstructure of eight new advanced RAFM steels subjected to TMTs and tempered at 750 °C during 2 h have been investigated. The major findings are summarized as follows.

- Ausforming has produced elongated prior austenite grains with very high dislocation density. Few primary precipitates were observed within of sub-grain of martensite laths nucleated at dislocations.
- Reduction of C content from 0.1010 wt% to 0.0820 wt% seems to be effective to reduce the size and amount of $M_{23}C_6$.
- The M_2X precipitation seems to be favored over MX when N contents between 0.03 and 0.04 wt% and V concentrations of approximately 0.2 wt%. This phase also precipitate with lower V contents (<0.2 wt %) with N concentrations ≥0.2 wt%.
- The formation of V-rich particles during tempering at 750 °C for 2 h after TMTs seems to be enhanced with V contents around 0.2 wt% and N concentrations in the range from 0.015 to 0.026 wt%.

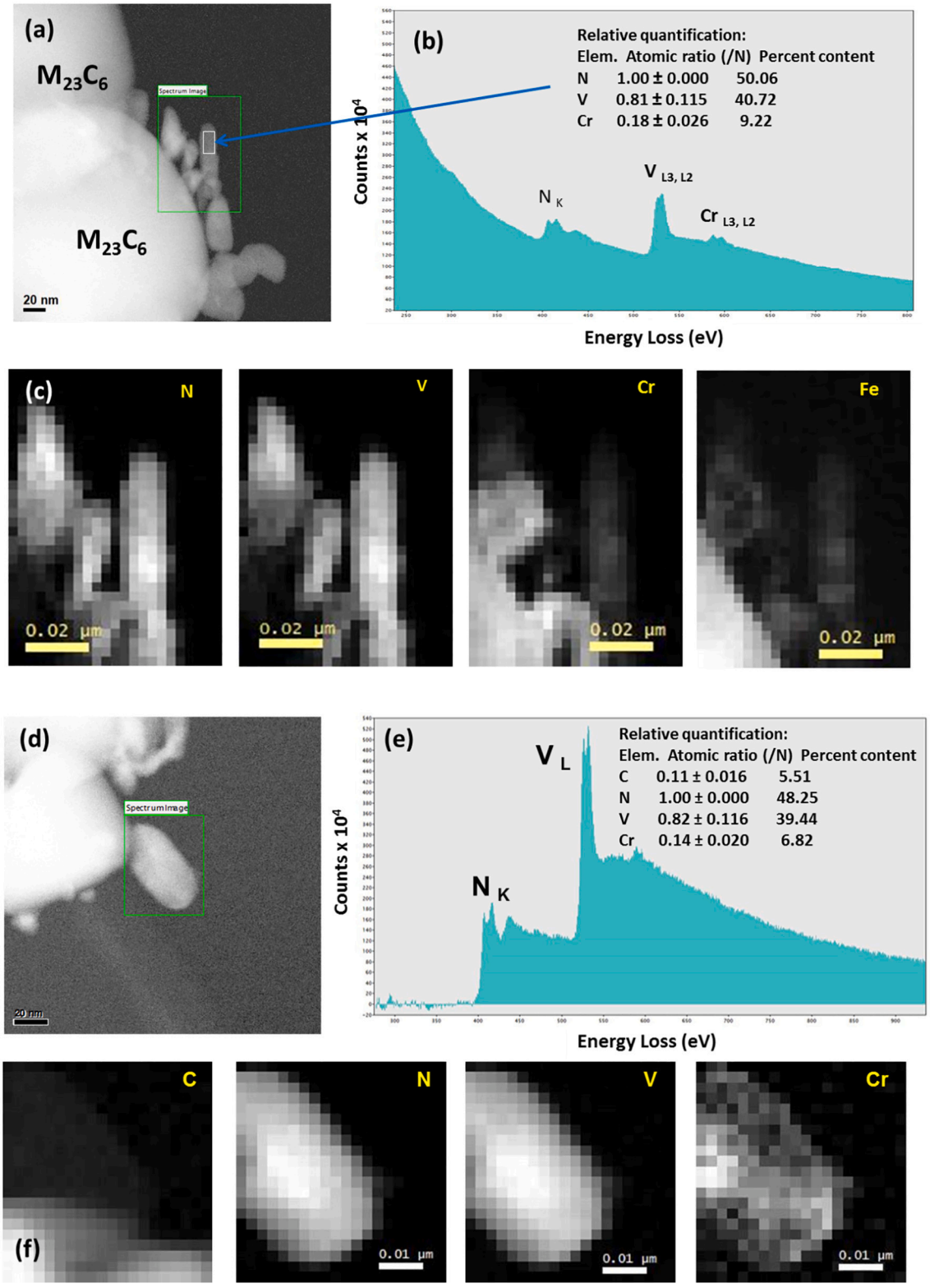

Fig. 11. Representative EELS analysis of V-rich particles precipitated after tempering at 750 °C/2 h; a–c) show the HAADF image of pure VN on Alloy K465A, the corresponding EELS spectrum, and EELS mapping, respectively. HAADF micrograph and EELS analysis (d–f) of the V(C, N) on Alloy K468A.

Table 4
Estimation of N/C and C/N ratios on MX phases detected in the eight Alloys investigated in this work.

Alloy	MX-V	MX-Ta	MX-Ti	Core-Shell
K465A	Pure VN	Very few		
	V(C,N) ⇒ N/C ~ 3–4	Ta (C,N) ⇒ N/C ~ 3.5		
K468A	V(C,N) ⇒ N/C ~ 3–4	Ta (C,N) ⇒ N/C ~ 5		
	V(C,N) ⇒ N/C ~ 6–8	Ta (C,N) ⇒ N/C ~ 2		
K473A	V(C,N) ⇒ N/C ~ 2	Ta (C,N) ⇒ C/N ~ 2	Ti (C,N) ⇒ N/C ~ 2–3.5	Core (Ti) ⇒ N/C ~ 2
		Ta (C,N) ⇒ N/C ~ 2		Shell (V) ⇒ N/C ~ 2
				Core (Ti) ⇒ N/C ~ 2
				Shell (Ta) ⇒ C/N ~ 2–3
K476A	V(C,N) ⇒ N/C ~ 5	Ta (C,N) ⇒ N/C ~ 5		
		Ta (C,N) ⇒ N/C ~ 2		
K466A	V(C,N) ⇒ N/C ~ 4	Ta (C,N) ⇒ C/N ~ 1.5		
K469A	Not present	Ta (C,N) ⇒ C/N ~ 1		
		Ta (C,N) ⇒ N/C ~ 1.5–2		
K471A	Not present	Ta (C,N) ⇒ C/N ~ 1.5		
K474A	Not present	Ta (C,N) ⇒ C/N ~ 1.5–2	Ti (C,N) ⇒ N/C ~ 1.5	Core (Ti) ⇒ N/C ~ 2
				Shell (Ta) ⇒ C/N ~ 3

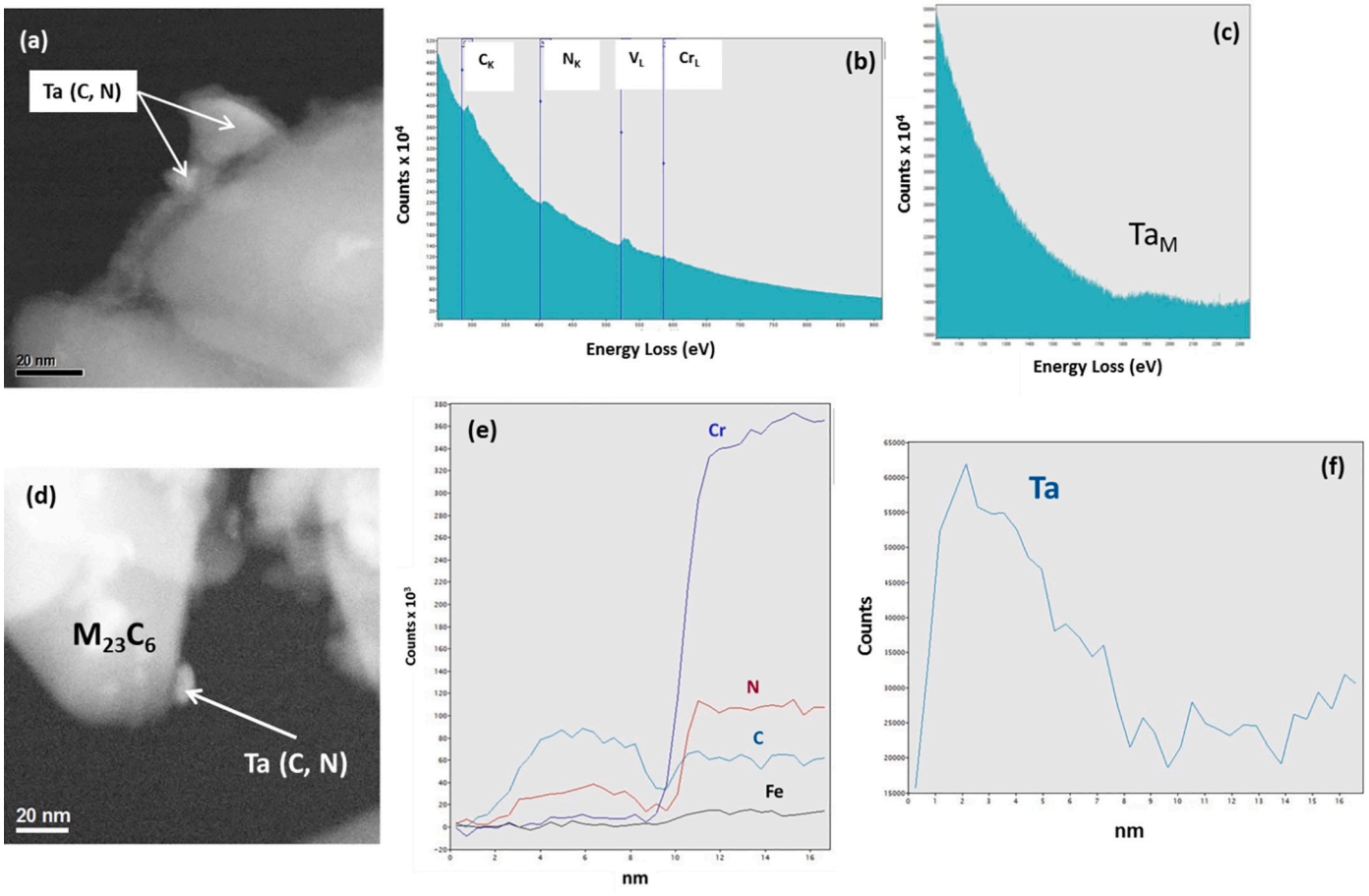

Fig. 12. Representative EELS analysis of Ta-rich particles precipitated after tempering at 750 °C/2 h; a–c) HAADF image and EELS spectrums of two Ta (C, N) analyzed on Alloy K469A, which present higher N than C, d–f) HAADF micrograph and EELS analysis of MX-Ta rich with higher C than N on Alloy K471A.

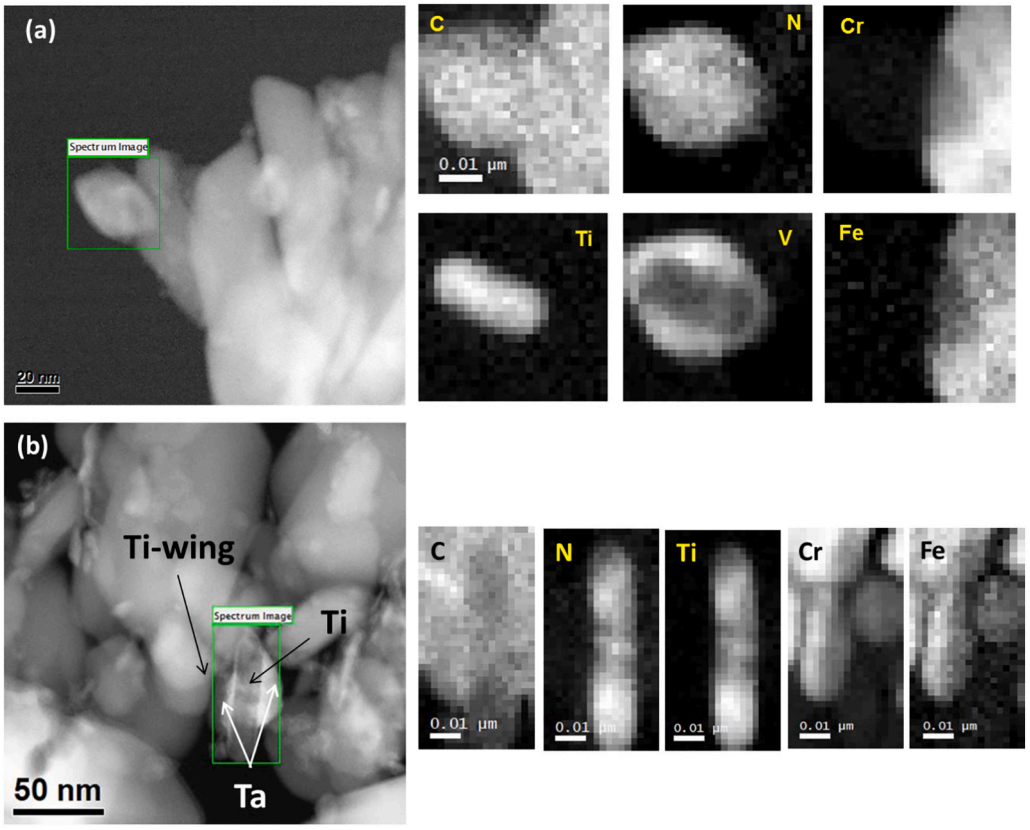

Fig. 13. Ti-rich particles precipitated after tempering at 750 °C/2 h; a) HAADF micrograph and EELS mapping of core (Ti)-shell (V) precipitates on Alloy K473A, and b) HAADF image and EELS mapping of Ti-wing on Alloy K474A. The Ta content in the wings was confirmed by EDS.

- Ti addition increases the number density of secondary phases, but with sizes larger than MX (Ta or V rich) and M_2X.
- EELS analysis have shown that the MX (Ta, V and Ti) precipitated after tempering at 750 °C for 2 h are mainly carbo-nitrides. Only, a few pure VN and TaC was detected on Alloy K465A.

Declaration of Competing Interest

The authors declare that they have no known competing financial interests or personal relationships that could have appeared to influence the work reported in this paper.

Acknowledgment

This work has been carried out within the framework of the EUROfusion Consortium and has received funding from the Euratom Research and Training Programme 2014–2018 and 2019–2020 under grant agreement No 633053. The views and opinions expressed herein do not necessarily reflect those of the European Commission.

References

[1] G.J. Butterworth, O.N. Jarvis, J. Nucl. Mater. 122–123 (1984) 982–988.
[2] R.L. Klueh, E.E. Bloom, Nucl. Eng. Des. Fusion 2 (1985) 383–389.
[3] D. Dulieu, K.W. Tupholme, G.J. Butterworth, J. Nucl. Mater. 141–143 (1986) 1067–1073.
[4] M. Tamura, H. Hatyakawa, M. Tanimura, A. Hishimuna, T. Kondo, J. Nucl. Mater. 141–143 (1986) 1067–1073.
[5] T. Noda, F. Abe, H. Araki, M. Okada, J. Nucl. Mater. 141–143 (1986) 1102–1106.
[6] M. Yamanouchi, M. Tamura, H. Hayakawa, A. Hishinuma, T. Kondo, J. Nucl. Mater. 191-94 (1992) 822–826.
[7] A. Kohyama, Y. Kohno, K. Asakura, An Kayano, J. Nucl. Mater. 22–215 (1994) 684–689.
[8] K. Anderko, K. Ehrlich, L. Schaefer, M. Schirra, CETA, a step towards a low activation martensitic steel, in: Technical Report KFK–5060, 1993.
[9] K. Ehrlich, S. Kelzenberg, H.D. Röhrig, L. Schäfer, M. Schira, J. Nucl. Mater. 212–215 (1994) 678–683.
[10] Q. Huang, N. Baluc, Y. Dai, S. Jitsukawa, A. Kimura, J. Konys, R.J. Kurtz, R. Lindau, T. Muroga, G.R. Odette, B. Raj, R.E. Stoller, L. Tan, H. Tanigawa, A. F. Tavassoli, T. Yamamoto, F. Wan, Y. Wu, J. Nucl. Mater. 442 (2013) 52–58.
[11] A.-A.F. Tavassoli, E. Diegele, R. Lindau, N. Luzginova, H. Tanigawa, J. Nucl. Mater. 455 (2014) 269–276.
[12] H. Tanigawa, K. Shiba, A. Moeslang, R.E. Stoller, R. Lindau, M.A. Sokolov, G. R. Odette, R.J. Kurtz, S. Jitsukawa, J. Nucl. Mater. 417 (2011) 9–15.
[13] R.W. Honeycombe, H.K.D.H. Bhadeshia, Steels-Microstructure and Properties, 2nd ed., Edward Arnold, London, 1995.
[14] W.B. Jones, C.R. Hills, D.H. Poloni, Metall. Trans. A. 22 (1991) 1049–1058.
[15] F.W. Noble, B.A. Senior, B.L. Eyre, Acta Metall. Mater. 38 (1990) 709–717.
[16] F. Brühl, H. Cerjak, P. Schwaab, H. Weber, Steel Res. 62 (1991) 75–82.
[17] J.G. Zhang, F. Noble, B.L. Eyre, Mater. Sci. Technol. 7 (1991) 218–223.
[18] F. Abe, H. Araki, T. Noda, Mater. Sci. Technol. (1992) 767–773.
[19] H. Finkler, M. Schirra, Steel Res. 67 (1996) 328–342.
[20] V. Vodárek, Z. Kuboň, V. Foldyna, Hutnické Listy 52 (4) (1997) 31–38.
[21] J. Janovec, B. Richarz, H.J. Grabke, Steel Res. 65 (1994) 438–443.
[22] R.C. Thomson, H.K.D. Bhadesia, Metall. Trans. A. 23 (1992) 1171–1179.
[23] F. Abe, H. Araki, T. Noda, Metall. Trans. A. 22 (1991) 2225–2235.
[24] R.L. Klueh, N. Hashimoto, P.J. Maziasz, Scr. Mater. 53 (2005) 275–280.
[25] L. Tan, J.T. Busby, P.J. Maziasz, Y. Yamamoto, J. Nucl. Mater. 441 (2013) 713–717.
[26] S. Hollner, B. Fournier, J. Le Pendu, T. Cozzika, I. Tournié, J.-C. Brcahet, A. Pineau, J. Nucl. Mater. 405 (2010) 101–108.
[27] L. Tan, D.T. Hoelzer, J.T. Busby, M.A. Sokolov, R.L. Klueh, J. Nucl. Mater. 422 (2012) 45–50.
[28] L. Tan, Y. Yang, J.T. Busby, J. Nucl. Mater. 442 (2013) 513–517.
[29] M. Song, C. Sun, Z. Fan, Y. Chen, R. Zhu, K.Y. Yu, K.T. Harwig, H. Wang, X. Zhang, Acta Mater. 112 (2016) 361–377.
[30] X. Zhou, Ch. Liu, L. Yu, Y. Liu, H. Li, J. Mater. Sci. Technol. 31 (2015) 235–242.
[31] L. Tan, L.L. Snead, Y. Katoh, J. Nucl. Mater. 478 (2016) 42–49.
[32] L. Tan, C.M. Parish, X. Hu, J. Nucl. Mater. 509 (2018) 267–275.
[33] R. Lindau, A. Möslang, M. Rieth, M. Klimiankov, E. Materna-Morris, A. Alamo, A.A. F. Tavassoli, C. Caryon, A.-M. Lancha, P. Fernández, N. Baluc, R. Schäublin, E. Diegele, G. Filacchioni, J.W. Rensman, B. van der Scaaf, E. Lucon, W. Dietz, Fusion Eng. Des. 75–79 (2005) 989–996.
[34] B. Uhrenius, S. Frondell, Met. Sci. 11 (1977) 73–81.
[35] Z. Naqiong, H. Yanlin, L. Wenqing, et al., J. Mater. Sci. Technol. 27 (2011) 725–728.
[36] D.H. Jack, K.H. Jack, Mater. Sci. Eng. 11 (1973) 1–27.

[37] X. Xiao, G. Liu, B. Hu, J. Wang, A. Ullah, Mater. Charact. 82 (2013) 130–139.
[38] R. Mythili Ravikirana, S. Raju, S. Satoja, T. Jayakumar, E. Rajendrakumar, Mater. Charact. 84 (2013) 196–204.
[40] F. Abe, Sci. Technol. Adv. Mater. 9 (2008), 013002.
[41] Jh. Zhou, Yf. Shen, N. Jia, Strengthening mechanisms of reduced activation ferritic/martensitic steels: a review, Int. J. Miner. Metall. Mater. 28 (2021) 335–348.
[42] F. Abe, M. Taneike, K. Sawada, Int. J. Press. Vessel. Pip. 84 (2007) 3–12.
[43] N. Taneike, N. Fujitsuna, F. Abe, Mater. Sci. Technol. 20 (2004) 1455–1461.
[44] K. Suzuki, S. Kumai, Y. Toda, H. Kushima, K. Kimura, ISIJ Int. 43 (2003) 1089–1094.
[45] P. Fernández, J. Hoffmann, M. Rieth, M. Roldán, A. Gómez-Herrero, J. Nucl. Mater. 500 (2018) 1–10.
[47] A. Bhattacharya, C.M. Parish, J. Henry, Y. Katoh, Ultamicroscopy 202 (2019) 33–43.
[48] P. Hofer, H. Cerjak, B. Schaffernak, P. Warbichler, Steel Res. 69 (1998) 343–348.
[49] A. Strang, V. Vodarek, Microstructural Stability of Creep Resistant Alloys for High-Temperature Plant Applications, The Inst. Of Materials, London, 1998, p. 117.
[50] K. Sawada, K. Suzuki, H. Kushima, M. Tabuchi, K. Kimura, Mat. Sci. Eng. A 480 (2008) 558–563.